Proceedings of the ASME Turbo Expo 2020: Turbine Technical Conference and Exposition
GT2020
June 22-26, 2020, London, UK

GT2020-14929

ASSIMILATION OF EXPERIMENTAL DATA TO CREATE A QUANTITATIVELY-ACCURATE REDUCED ORDER THERMOACOUSTIC MODEL

Francesco Garita*
Department of Engineering
University of Cambridge
Cambridge, United Kingdom CB21PZ
Email: fg372@cam.ac.uk

Hans Yu
Department of Engineering
University of Cambridge
Cambridge, United Kingdom CB21PZ
Email: hy313@cam.ac.uk

Matthew P. Juniper
Department of Engineering
University of Cambridge
Cambridge, United Kingdom CB21PZ
Email: mpj1001@cam.ac.uk

ABSTRACT

We combine a thermoacoustic experiment with a thermoacoustic reduced order model using Bayesian inference to accurately learn the parameters of the model, rendering it predictive. The experiment is a vertical Rijke tube containing an electric heater. The heater drives a base flow via natural convection, and thermoacoustic oscillations via velocity-driven heat release fluctuations. The decay rates and frequencies of these oscillations are measured every few seconds by acoustically forcing the system via a loudspeaker placed at the bottom of the tube. More than 320,000 temperature measurements are used to compute state and parameters of the base flow model using the Ensemble Kalman Filter. A wave-based network model is then used to describe the acoustics inside the tube. We balance momentum and energy at the boundary between two adjacent elements, and model the viscous and thermal dissipation mechanisms in the boundary layer and at the heater and thermocouple locations. Finally, we tune the parameters of two different thermoacoustic models on an experimental dataset that comprises more than 40,000 experiments. This study shows that, with thorough Bayesian inference, a qualitative model can become quantitatively accurate, without overfitting, as long as it contains the most influencial physical phenomena.

*Address all correspondence to this author.

NOMENCLATURE

A_g	Cross-sectional area of gas [m^2], $A_\mathrm{g} = \pi D^2/4$
A_s	Cross-sectional area of solid wall [m^2], $A_\mathrm{s} = \pi\varepsilon(D+\varepsilon)$
c	Speed of sound propagation [m s^{-1}]
$c_{\mathrm{p,g}}$	Specific heat capacity of gas at constant pressure [m^2 s^{-2} K^{-1}]
c_s	Specific heat capacity of solid [m^2 s^{-2} K^{-1}]
d_f	Diameter of one of the heater filaments [m]
D	Internal diameter of tube [m]
D_p	Diameter of single prong [m]
D_w	Diameter of single wire [m]
D_Σ	Total diameter including two prongs and two wires (if present) [m], $D_\Sigma = D + 2(D_\mathrm{p} + D_\mathrm{w})$ or $D_\Sigma = D$
F	Friction force at the solid wall [N]
g	Acceleration of gravity [m s^{-2}]
h_i	Convective heat transfer coefficient from gas to solid [W m^{-2} K^{-1}]
h_o	Convective heat transfer coefficient from solid to ambient [W m^{-2} K^{-1}]
k_i	Inviscid pressure loss coefficient at the heater location, $k_\mathrm{i} = \Delta p / \left(\frac{1}{2}\rho_\mathrm{h} U_\mathrm{h}^2\right)$
L	Length of the tube [m]
n	Interaction index
Nu_i	Nusselt number for convective heat transfer from gas to solid, $\mathrm{Nu}_\mathrm{i} = h_\mathrm{i}\, D/\lambda_\mathrm{g}$
Nu_o	Nusselt number for convective heat transfer from solid to ambient, $\mathrm{Nu}_\mathrm{o} = h_\mathrm{o} L/\lambda_\mathrm{a}$

p Gas pressure [Pa]
Pr Prandtl number, $\mathrm{Pr} = \rho_g \nu c_{p,g}/\lambda_g$
$\dot{q}/\dot{Q}$ Thermal power [W]
$\dot{Q}_i$ Thermal power from gas to solid [W], $\dot{Q}_i = h_i \pi_i (T_g - T_s)\delta x$
$\dot{Q}_o$ Thermal power from solid to ambient [W], $\dot{Q}_o = h_o \pi_o (T_s - T_a)\delta x$
R Reflection coefficient
R_g^* Gas constant of air [$m^2\ s^{-2}\ K^{-1}$], $R_g^* = p/(\rho T)$
s Complex frequency of the thermoacoustic system [s^{-1}], $s = s_r + i\, s_i$
s_i Frequency of oscillation [s^{-1}]
s_r Growth/Decay rate of oscillation [s^{-1}]
t Time [s]
T Temperature [K]
u/U Gas velocity [$m\ s^{-1}$]
x Axial coordinate [m]

γ Heat capacity ratio of air, $\gamma = 1.4$
δ_{bl} Boundary layer thickness [m]
Δx Length of small acoustic element [m]
ε Tube thickness [m]
Θ^* Non-dimensional temperature, $\Theta^* = (T - T_1)/T_1$
λ Thermal conductivity [$W\ m^{-1}\ K^{-1}$]
ν Momentum diffusivity [$m^2\ s^{-1}$]
π_i Inner perimeter of solid wall [m], $\pi_i = \pi D$
π_o Outer perimeter of solid wall [m], $\pi_o = \pi(D + 2\varepsilon)$
ρ Density [$kg\ m^{-3}$]
τ Time delay [s]
τ_{wall} Shear stress at the tube wall [$kg\ m^{-1}\ s^{-2}$]

$\overline{(\cdot)}$ Average gas quantity
$\tilde{(\cdot)}$ Quantity per unit length
$(\cdot)^*$ Non-dimensional quantity
$(\cdot)'$ First-order perturbed quantity
$(\cdot)_1$ Geometric or gas quantity evaluated at tube inlet section
$(\cdot)_2$ Geometric or gas quantity evaluated at tube outlet section
$(\cdot)_a$ Quantity at ambient conditions
$(\cdot)_d$ Quantity downstream of heater
$(\cdot)_{dd}$ Quantity referring to drag device
$(\cdot)_e$ Equivalent quantity
$(\cdot)_g$ Quantity that refers to gas
$(\cdot)_h$ Quantity that refers to heater or evaluated at heater location
$(\cdot)_i$ Quantity that refers to acoustic element i
$(\cdot)_m$ Quantity that refers to microphone
$(\cdot)_p$ Quantity that refers to a single heater prong
$(\cdot)_s$ Quantity that refers to solid wall
$(\cdot)_t$ Quantity that refers to thermocouple
$(\cdot)_{th}$ Thermal quantity
$(\cdot)_u$ Quantity upstream of heater
$(\cdot)_{vis}$ Viscous quantity
$(\cdot)_w$ Quantity that refers to a single heater wire

1 INTRODUCTION

Thermoacoustic oscillations are nonlinear phenomena that occur whenever heat release rate fluctuations are sufficiently in phase with pressure oscillations. They can cause structural vibration of the system or even complete destruction. Predicting and eliminating thermoacoustic oscillations is a significant challenge in gas turbine design. Due to the high sensitivity of the growth rate of oscillations to geometry, boundary conditions, and system parameters, models often fail at accurately predicting the instability of a thermoacoustic system. This means that a stable lab-scale engine does not guarantee that its full-scale version will be stable as well. An example of this is the Saturn V engine, which required more than 2000 full-scale tests before a stable configuration was achieved [1]. Recently introduced legislation regarding NO_x emission [2], will require gas turbines to operate at lean premixed conditions. These conditions, however, are more conducive to thermoacoustic instability because lean flames are more sensitive to equivalence ratio perturbations [2–4]. This motivates research into quantitative modelling of these phenomena.

The goal of this study is to combine statistical methods with a vast amount of experimental data in order to extract quantitatively-accurate reduced order models based on physical principles. This technique is called data assimilation, and was first developed for meteorology problems [5]. The problem of having a computational model that depends on parameters with unknown value and uncertainty represents a classical inverse problem. Many engineering problems fall into this category, and therefore many mathematical tools have been developed for this over the past decades. In the first part of this study the unknown parameters are inferred using an Ensemble Kalman Filter (EnKF), which is a data assimilation technique, whereas in the second part we infer the model parameters by simple regression.

The paper is organized as follows. Sec. 2 provides a description of the physical mechanism that triggers thermoacoustic instabilities in a Rijke tube. Sec. 3 describes the experimental apparatus and the way data are acquired and processed. Sec. 4 presents a model of the base flow that arises by natural convection inside the Rijke tube, and describes how this is combined with the experimental observations. Sec. 5 contains details on the acoustic model, which is built using the information coming from the base flow model. Sec. 6 tests and compares two different physics-based thermoacoustic models.

2 PHYSICAL DESCRIPTION OF THE RIJKE TUBE

In this study we use a Rijke tube, which is a simple thermoacoustic device that supports thermoacoustic oscillations. It

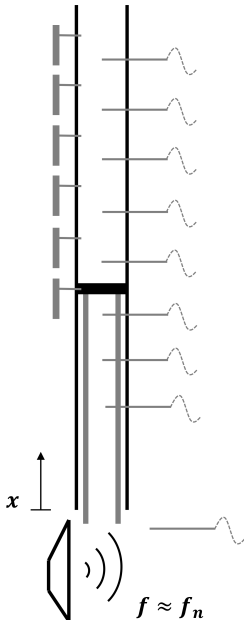

FIGURE 1: Sketch of the experimental apparatus including 6 microphones, 8 thermocouples to measure the gas temperature at the tube centerline, a thermocouple to measure the ambient temperature, a loudspeaker, and an electric heater held in place by a pair of prongs and wires. Note that the loudspeaker acoustically forces the system at a frequency, f, close to the natural frequency of the tube, f_n.

is a vertical tube, generally open at both ends, which contains a heat source. The heat source sets up a natural convection flow through the tube. On top of the mean flow, small acoustic perturbations can propagate. For a tube open at both ends, the first acoustic mode has a pressure node and a velocity antinode at the two ends of the tube, and a pressure antinode and a velocity node in the middle. Air flows towards the centre of the tube during the compression phase of an acoustic cycle and away from the centre during the expansion phase. When the heat source is placed in the bottom half of the tube, it experiences a higher-than-average velocity during the compression phase, which increases the heat transfer to the flow, and a lower-than-average velocity during the expansion phase, which decreases the heat transfer to the flow. Typically there is also a small time delay between the velocity perturbation and the subsequent heat transfer perturbation. The time delay is such that moments of increased heat transfer occur during moments of increased pressure, and moments of decreased heat transfer occur during moments of decreased pressure. In the absence of dissipation, this causes the acoustic energy to grow [6]. In the presence of dissipation, typically through visco-thermal mechanisms and acoustic radiation, the acoustic energy grows only if the above driving mechanism

FIGURE 2: Electric heater made up of 0.559 mm diameter Ni-Cr filaments wound between two parallel ceramic rings.

exceeds the dissipation. Ref. [7] found that the optimal position for self-excited thermoacoustic oscillations is when the heat source is placed at $x_\mathrm{h}/L = 0.25$. When the heat source is instead placed in the top half of the tube, moments of increased heat transfer coincide with moments of lower pressure, and moments of decreased heat transfer coincide with moments of higher pressure. This causes the acoustic energy to decrease [6].

3 EXPERIMENTAL SETUP

3.1 Apparatus

A sketch of the experimental apparatus is shown in Fig. 1. The rig consists of a 1 m long stainless steel vertical tube with an internal diameter of 47.4 mm and a wall thickness of 1.7 mm. An electric heater (Fig. 2) is attached to two rods and held in place at four different positions from the bottom end of the tube: $x_\mathrm{h}/L = [0.55, 0.50, 0.45, 0.40]$. The heater is powered by an Elektro-Automatik EA-PSI 5080-20 A DC programmable power supply with maximum power 640 W, controlled through National Instruments LabVIEW. The experimental apparatus, as described so far, is that in [8].

Six G.R.A.S. 40SA probe microphones are used to record the pressure near the inner surface of the tube at different axial locations measured from the bottom of the tube: $x_\mathrm{m}/L = [0.95, 0.85, 0.75, 0.65, 0.55, 0.45]$. Each microphone is equipped with a 20 mm long probe, on top of which a temperature shield is mounted. The raw pressure signal is sampled at 10 kHz, which is much higher than the anticipated frequencies of the thermoacoustic oscillations, 170 to 190 Hz. All data is acquired through a National Instruments BNC-2110 DAQ device using LabVIEW. A 4 Ω Visaton FRS 8 loudspeaker is fixed at the base of the tube. The loudspeaker is connected to a Stage Line STA-500 Pro

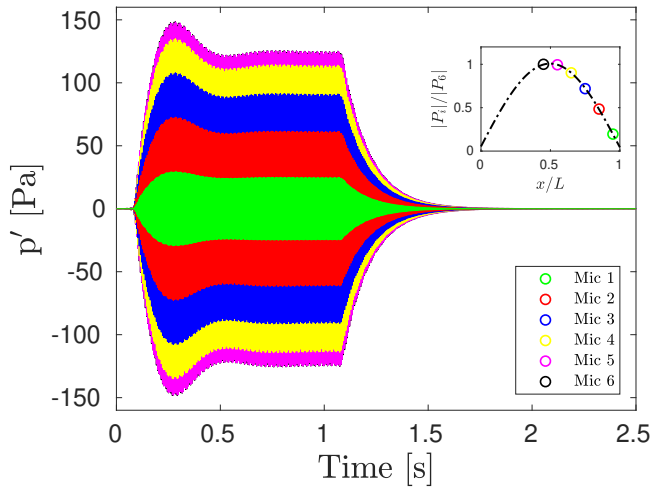

FIGURE 3: Pressure oscillations recorded by the six microphones after sinusoidal forcing at 170 Hz. The inset figure shows the corresponding pressure eigenmode.

Power amplifier with maximum power 600 W controlled through National Instruments LabVIEW.

Eight type-K thermocouples are installed along the centreline of the tube through small holes at positions $x_t/L = [0.90, 0.80, 0.70, 0.60, 0.50, 0.40, 0.30, 0.20]$. An additional thermocouple is placed near the inlet section to record the ambient temperature. All thermocouples are logged with four TC-08 USB DAQ boxes. In the following discussion, we will assume that the temperature does not vary in the radial direction, so that a 1D model can be used. This assumption could be relaxed, but the modelling would be significantly more expensive.

3.2 Data acquisition

The experiment is automated through National Instruments LabVIEW. The input power is varied in steps of 10 W, from 10 W to 180 W. Each step lasts 70 minutes. For every heater position, each experiment lasts 21 hours. The nine thermocouples measure the temperature simultaneously every 7 seconds. Every 7 seconds, a sinusoidal signal at 170 Hz is provided to the loudspeaker. At these heater powers, the system is thermoacoustically stable, so the acoustic oscillations decay. Their decay rate and frequency depend, however, on the thermoacoustic driving from the heater. The experimental campaign is carried out in the stable regime because the power that can be provided to the heater is limited to 300 W, which is not enough to acquire a large set of experimental data in the unstable regime. Investigation of the unstable regime would require an additional microphone to be placed near the top end of the tube, and a phase-shift amplifier for active control of the system.

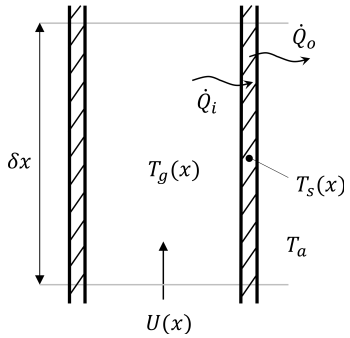

FIGURE 4: Sketch of a small element of tube of length δx with gas speed $U(x)$, gas temperature $T_g(x)$, solid temperature $T_s(x)$, ambient temperature T_a, and inner and outer heat flow rates $\dot{Q}_i$ and $\dot{Q}_o$, respectively.

3.3 Data processing

Fig. 3 shows a plot of the pressure signal recorded by the six microphones. To extract the decay rate and frequency, firstly, the decaying part of the signal is isolated. Secondly, the Fourier transform is applied. Thirdly, the logarithm of the resulting signal is taken. Finally, by means of a lifted cosine weighted function, a weighted least squares regression is performed in order to fit a straight line. The slope of the straight line corresponds to the decay rate, whereas the frequency of the oscillations is given by the frequency where the peak in the Fourier spectrum occurs. This procedure is applied to each microphone, and the six values are then averaged to obtain a more robust estimate, although no significant scatter exists between the six measurements. The averaged decay rate and frequency represent the real and imaginary parts of the complex frequency s, respectively.

4 BASE FLOW MODEL AND ANALYSIS

4.1 Model

We consider a small element of tube of length δx (see Fig. 4). The energy balance in the solid reads

$$(\rho_s A_s \delta x) c_s \frac{\partial T_s}{\partial t} = -\frac{\partial \dot{Q}_s}{\partial x}\delta x - \dot{Q}_o + \dot{Q}_i \qquad (1)$$

By assuming that the diffusive heat transfer $\dot{Q}_s = -\lambda_s \frac{\partial T_s}{\partial x}$, and that $\dot{Q}_o$ and $\dot{Q}_i$ can be modelled with convective heat transfer coefficients h_o and h_i, respectively, and by further assuming constant thermal conductivity λ_s, Eq. (1) can be re-written as

$$\rho_s A_s c_s \frac{\partial T_s}{\partial t} = \lambda_s A_s \frac{\partial^2 T_s}{\partial x^2} - h_o \pi_o (T_s - T_a) + h_i \pi_i (T_g - T_s) \qquad (2)$$

By re-arranging and replacing the convective heat transfer coefficients with Nusselt numbers, one obtains

$$\begin{aligned}\frac{\partial T_\mathrm{s}}{\partial t} = \frac{\lambda_\mathrm{s}}{\rho_\mathrm{s} c_\mathrm{s}} \frac{\partial^2 T_\mathrm{s}}{\partial x^2} - \mathrm{Nu_o} \frac{\lambda_\mathrm{a}}{\rho_\mathrm{s} c_\mathrm{s}} \frac{\pi_\mathrm{o}}{A_\mathrm{s} L} (T_\mathrm{s} - T_\mathrm{a}) \\ + \mathrm{Nu_i} \frac{\lambda_\mathrm{g}}{\rho_\mathrm{s} c_\mathrm{s}} \frac{\pi_\mathrm{i}}{A_\mathrm{s} D} (T_\mathrm{g} - T_\mathrm{s})\end{aligned} \tag{3}$$

The same procedure can be applied to a control volume containing gas moving at local speed U, thus giving

$$(\rho_\mathrm{g} A_\mathrm{g} \delta x) c_\mathrm{p,g} \left(\frac{\partial T_\mathrm{g}}{\partial t} + U \frac{\partial T_\mathrm{g}}{\partial x} \right) = -\frac{\partial \dot{Q}_\mathrm{g}}{\partial x} \delta x - \dot{Q}_\mathrm{i} + \tilde{\dot{Q}}_\mathrm{h} \delta x \tag{4}$$

In Eq. (4), the source term $\tilde{\dot{Q}}_\mathrm{h}$ accounts for the electric heater. The inlet gas quantities $(\cdot)_1$ are assumed to be ambient $(\cdot)_\mathrm{a}$. One can now apply the ideal gas law, as well as Fourier's law, and use mass conservation in its integral form $\left(\frac{\partial(\rho A U)}{\partial x} = 0\right)$, to obtain

$$\begin{aligned}\rho_1 A_\mathrm{g} c_\mathrm{p,g} \frac{T_1}{T_\mathrm{g}} \frac{\partial T_\mathrm{g}}{\partial t} + \rho_1 A_\mathrm{g} c_\mathrm{p,g} U_1 \frac{\partial T_\mathrm{g}}{\partial x} \\ = \lambda_\mathrm{g} A_\mathrm{g} \frac{\partial^2 T_\mathrm{g}}{\partial x^2} - \mathrm{Nu_i} \lambda_\mathrm{g} \frac{\pi_\mathrm{i}}{D} (T_\mathrm{g} - T_\mathrm{s}) + \tilde{\dot{Q}}_\mathrm{h}\end{aligned} \tag{5}$$

The gas thermal conductivity is assumed to be equal to that of air at ambient conditions, i.e. $\lambda_\mathrm{g} = \lambda_\mathrm{a} = \lambda_1$. Radiation is not modelled.

We also solve the integral momentum equation, in which we assume that (i) the unsteady term is negligible, i.e. the inertia forces are negligible compared with the buoyancy and drag forces, and (ii) the total pressure losses Δp are concentrated at the heater location, and modelled through an inviscid pressure loss coefficient k_i, such that $\Delta p = k_\mathrm{i}(\rho_\mathrm{h} U_\mathrm{h}^2)/2$. The integral momentum equation is

$$\rho_2 U_2^2 - \rho_1 U_1^2 + k_\mathrm{i} \frac{\rho_\mathrm{h} U_\mathrm{h}^2}{2} = \int_0^L (\rho_1 - \rho_\mathrm{g}) g \, \mathrm{d}x \tag{6}$$

By using mass conservation and the ideal gas law, Eq. (6) can be re-arranged to

$$U_1^2 \left[\frac{k_\mathrm{i}}{2} \left(\frac{A_1}{A_\mathrm{h}} \right)^2 \frac{T_\mathrm{h}}{T_1} + \left(\frac{A_1}{A_2} \right)^2 \frac{T_2}{T_1} - 1 \right] = \int_0^L \frac{(\rho_1 - \rho_\mathrm{g})}{\rho_1} g \, \mathrm{d}x \tag{7}$$

In our case $A_1 = A_2 = A_\mathrm{h}$, but in general these areas could be different.

4.2 Non-dimensionalization

We non-dimensionalize Eqs. (3), (5) and (7) with the reference scales $\{L,\ g,\ T_1\}$, which naturally give a time scale $(L/g)^{1/2}$, and a velocity scale $(gL)^{1/2}$. Temperatures are measured relative to T_1 and then divided by T_1. For example, T becomes $\Theta^* = \frac{T - T_1}{T_1}$. Non-dimensional quantities are denoted by $(\cdot)^*$ to distinguish them from the corresponding dimensional quantities. The energy equation for the solid becomes

$$\begin{aligned}\frac{T_1}{(L/g)^{1/2}} \frac{\partial \Theta_\mathrm{s}^*}{\partial t^*} = \frac{\lambda_\mathrm{s}}{\rho_\mathrm{s} c_\mathrm{s}} \frac{T_1}{L^2} \frac{\partial^2 \Theta_\mathrm{s}^*}{\partial x^{*2}} \\ - \mathrm{Nu_o} \frac{\lambda_\mathrm{a}}{\rho_\mathrm{s} c_\mathrm{s}} \frac{\pi_\mathrm{o}}{A_\mathrm{s} L} T_1 \Theta_\mathrm{s}^* + \mathrm{Nu_i} \frac{\lambda_\mathrm{a}}{\rho_\mathrm{s} c_\mathrm{s}} \frac{\pi_\mathrm{i}}{A_\mathrm{s} D} T_1 (\Theta_\mathrm{g}^* - \Theta_\mathrm{s}^*)\end{aligned} \tag{8}$$

We define the following non-dimensional parameters

$$\eta_1^* = \frac{1}{L(gL)^{1/2}} \frac{\lambda_\mathrm{s}}{\rho_\mathrm{s} c_\mathrm{s}} \tag{9}$$

$$\eta_2^* = \frac{\pi_\mathrm{o}}{A_\mathrm{s}(gL)^{1/2}} \frac{\lambda_\mathrm{a}}{\rho_\mathrm{s} c_\mathrm{s}} \tag{10}$$

$$\eta_3^* = \frac{\pi_\mathrm{i}}{A_\mathrm{s}(gL)^{1/2}} \frac{L}{D} \frac{\lambda_\mathrm{a}}{\rho_\mathrm{s} c_\mathrm{s}} \tag{11}$$

and re-write Eq. (8) compactly as

$$\frac{\partial \Theta_\mathrm{s}^*}{\partial t^*} = \eta_1^* \frac{\partial^2 \Theta_\mathrm{s}^*}{\partial x^{*2}} - \mathrm{Nu_o} \eta_2^* \Theta_\mathrm{s}^* + \mathrm{Nu_i} \eta_3^* (\Theta_\mathrm{g}^* - \Theta_\mathrm{s}^*) \tag{12}$$

The energy equation for the gas becomes

$$\begin{aligned}\rho_\mathrm{a} A_\mathrm{g} c_\mathrm{p,g} \frac{T_1}{(L/g)^{1/2}} \frac{1}{(\Theta_\mathrm{g}^* + 1)} \frac{\partial \Theta_\mathrm{g}^*}{\partial t^*} \\ + \rho_\mathrm{a} A_\mathrm{g} c_\mathrm{p,g} \frac{T_1}{(L/g)^{1/2}} U_1^* \frac{\partial \Theta_\mathrm{g}^*}{\partial x^*} = \lambda_\mathrm{a} A_\mathrm{g} \frac{T_1}{L^2} \frac{\partial^2 \Theta_\mathrm{g}^*}{\partial x^{*2}} \\ - \mathrm{Nu_i} \lambda_\mathrm{a} \frac{\pi_\mathrm{i}}{D} T_1 (\Theta_\mathrm{g}^* - \Theta_\mathrm{s}^*) + \tilde{\dot{Q}}_\mathrm{h}\end{aligned} \tag{13}$$

We define the following non-dimensional parameters

$$\eta_4^* = \frac{1}{L(gL)^{1/2}} \frac{\lambda_\mathrm{a}}{\rho_\mathrm{a} c_\mathrm{p,g}} \tag{14}$$

$$\eta_5^* = \frac{\pi_\mathrm{i}}{A_\mathrm{g}(gL)^{1/2}} \frac{L}{D} \frac{\lambda_\mathrm{a}}{\rho_\mathrm{a} c_\mathrm{p,g}} \tag{15}$$

$$\dot{Q}_\mathrm{h}^* = \frac{(L/g)^{1/2}}{T_\mathrm{l}} \frac{\tilde{\dot{Q}}_\mathrm{h}}{\rho_\mathrm{a} A_\mathrm{g} c_\mathrm{p,g}} \tag{16}$$

and re-write Eq. (13) compactly as

$$\frac{1}{(\Theta_\mathrm{g}^* + 1)} \frac{\partial \Theta_\mathrm{g}^*}{\partial t^*} + U_\mathrm{l}^* \frac{\partial \Theta_\mathrm{g}^*}{\partial x^*} = \eta_4^* \frac{\partial^2 \Theta_\mathrm{g}^*}{\partial x^{*2}} - \mathrm{Nu_i} \eta_5^* (\Theta_\mathrm{g}^* - \Theta_\mathrm{s}^*) + \dot{Q}_\mathrm{h}^* \tag{17}$$

The integral momentum equation becomes

$$\int_0^1 \frac{\Theta_\mathrm{g}^*}{\Theta_\mathrm{g}^* + 1} \mathrm{d}x^* = U_\mathrm{l}^{*2} \left[\frac{k_\mathrm{i}}{2} \left(\frac{A_1}{A_\mathrm{h}} \right)^2 (\Theta_\mathrm{h}^* + 1) + \left(\frac{A_1}{A_2} \right)^2 (\Theta_2^* + 1) - 1 \right] \tag{18}$$

4.3 Numerical implementation

A 1D Finite-Difference scheme with 101 points is used for spatial discretization of the base flow model. The scheme is fourth-order accurate and is centred everywhere except at the boundaries, where it is biased. Zero temperature gradients are imposed at the inlet and outlet boundaries. An explicit fourth-order accurate Runge-Kutta scheme is used for time integration. The source term in Eq. (17), $\dot{Q}_\mathrm{h}^*$, is modelled with a Gaussian distribution centred at the heater location, with variance set arbitrarily to 0.0002 m^2, normalized such that its integral equals the input power. The second-order accurate midpoint rule is used for the integral in Eq. (18).

4.4 Bayesian inference

The 1D unsteady model is marched forward in time to reproduce the evolution of the experiment. This, however, requires knowledge of the three parameters $\mathrm{Nu_i}$, $\mathrm{Nu_o}$, and k_i. We wish to exploit the information from both the model and the experiments in order to obtain the best possible estimate of the gas and solid temperature profiles. We must consider that our base flow model is nonlinear in the temperature Θ_g^*. The Ensemble Kalman Filter is a suitable tool to address these problems [5]. This represents the statistically optimal method when working with Gaussian distributions of state and parameters, in the sense that it provides the minimum variance estimate or, equivalently, the maximum likelihood estimate of $f(\boldsymbol{\psi}|\mathbf{d})$ [5]. The idea, which relies on Bayes' theorem, is to find the optimal estimate for state and parameters, given the marginal probability of the model $\big($often called the *prior*, $f(\boldsymbol{\psi})\big)$, which is the probability of the model with no knowledge of the data, and the probability of the data given the model $\big($often called the *likelihood* function, $f(\boldsymbol{d}|\boldsymbol{\psi})\big)$. The product of these two probability density functions, once properly normalized, gives the probability of the model given the data $\big($often called the *posterior*, $f(\boldsymbol{\psi}|\mathbf{d})\big)$, which represents the statistically best estimate that one can compute, given the model and the experimental data with the associated uncertainties. This is summarized by $f(\boldsymbol{\psi}|\mathbf{d}) = \frac{f(\boldsymbol{\psi}) f(\boldsymbol{d}|\boldsymbol{\psi})}{f(\boldsymbol{d})}$, which represents Bayes' theorem. In the present case, the state is a vector containing the solid and gas temperatures at every grid point, and the parameters are $\mathrm{Nu_i}$, $\mathrm{Nu_o}$, and k_i.

The EnKF randomly samples from the prior distributions and simulates every member of this ensemble until experimental observations become available. The prior distributions of the state and the parameters are defined by their mean and standard deviations. We set the initial state to be the ambient state with zero variance. We set the initial parameters $[\mathrm{Nu_i}, \mathrm{Nu_o}, k_\mathrm{i}]^T$ arbitrarily to have mean $[7, 60, 9.5]^T$ and variance $[0.2, 0.3, 0.1]^T$. We assume that the experimental temperature measurements have uncertainty ± 4 K. We use an ensemble made up of 30 members. Once the temperature measurements become available (every 7 seconds), state and parameters are updated using Bayes' theorem. Because the model is nonlinear, the initial Gaussian shape of the prior distribution deforms into a non-Gaussian distribution. Before the update step, the mean and covariance of this new distribution are computed from the ensemble members and a new Gaussian distribution is assumed, with the same mean and covariance. The update state is performed and the optimal state and parameters are estimated with their uncertainties, based on the likelihood function. The optimal distributions then become the new prior distributions to sample from, and the process repeats. With this process, one is able to (i) infer the evolution of the model parameters with their uncertainties, and (ii) improve the estimate of the state, which becomes more robust by learning from the experimental measurements.

4.5 Analysis

Figs. 5a to 5c show the evolution of the model parameters from low powers (10 W) to high powers (180 W), with an uncertainty of $\pm 2\sigma$. The results for $x_\mathrm{h}/L = [0.40, 0.50]$ have higher uncertainties and less regular trends than those for $x_\mathrm{h}/L = [0.45, 0.55]$ especially as far as $\mathrm{Nu_i}$ is concerned. This is because for $x_\mathrm{h}/L = [0.40, 0.50]$ the thermocouple measurements at the heater location are affected by radiation and conduction, and are therefore discarded, being these mechanisms not included in our model. This is the most informative location (see Fig. 5e). Fig. 5d shows the inlet bulk velocity, which increases to a plateau at high powers. Despite the imperfection

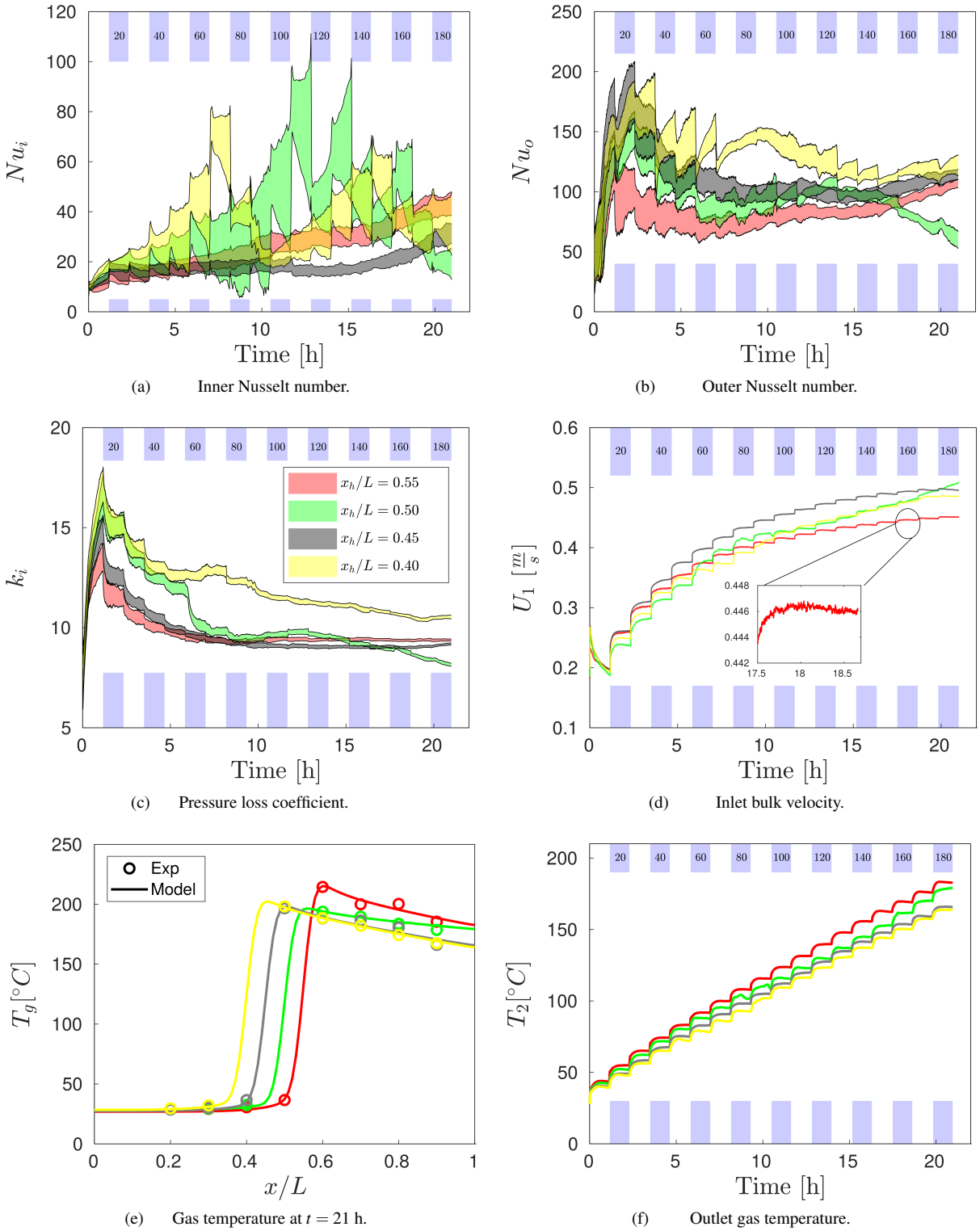

(a) Inner Nusselt number.

(b) Outer Nusselt number.

(c) Pressure loss coefficient.

(d) Inlet bulk velocity.

(e) Gas temperature at $t = 21$ h.

(f) Outlet gas temperature.

FIGURE 5: (a), (b), (c): Base flow model parameters with uncertainty $\pm 2\sigma$ as functions of time ([h], bottom axis) or heater power ([W], top axis). (d): Bulk velocity of the gas at the inlet of the tube. (e) Gas temperature distribution inside the tube at $t = 21$ h ($\dot{Q}_{\text{h}} = 180$ W) with corresponding experimental measurements. (f) Outlet gas temperature evolution.

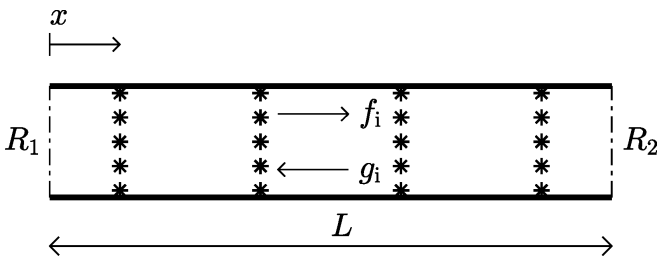

FIGURE 6: Sketch of a network model with five acoustic elements separated by four jump conditions. The travelling waves in each acoustic element are denoted by f_i and g_i. R_1 and R_2 are the inlet and outlet reflection coefficients.

in the model, the gas temperature (Fig. 5e) seems to capture well the experiments even for the largest discrepancy case ($\dot{Q}_h = 180$ W). Finally, Fig. 5f shows the evolution of the outlet gas temperature, which is particularly influential for the phase of the outlet reflection coefficient.

5 ACOUSTIC MODEL AND ANALYSIS

5.1 Model

To model the acoustics, we split the domain into 50 acoustic elements, each with constant density, pressure, and temperature, and connect these with a network model [9]. Forces (shear stress at the wall) and heat transfer (to and from the wall) are integrated across adjacent acoustic elements and then modelled by jump conditions between the elements. The choice of using 50 acoustic elements is simply motivated by the fact that a smaller number does not significantly reduce the computational cost. Fig. 6 shows a sketch of a network model with five acoustic elements separated by four *drag devices*, denoted by $(\cdot)_{dd}$, representing four jump conditions. We assume that entropy waves have no influence and, knowing that the mean flow is much slower than the speed of sound, assume zero mean flow. The linearized momentum and energy equations in each acoustic element are

$$\overline{\rho}\frac{\partial u'}{\partial t} + \frac{\partial p'}{\partial x} = 0 \tag{19}$$

$$\frac{\partial p'}{\partial t} + \gamma\overline{p}\frac{\partial u'}{\partial x} = 0 \tag{20}$$

The solution of the above equations is obtained by performing a Riemann decomposition, which results in a f-wave travelling downstream and a g-wave travelling upstream. The pressure and the velocity fluctuations in the generic acoustic element i are

$$p'_i(x,t) = f_i\left(t - \frac{x}{\overline{c}_i}\right) + g_i\left(t + \frac{x}{\overline{c}_i}\right) \tag{21}$$

$$u'_i(x,t) = \frac{1}{\overline{\rho}_i\overline{c}_i}\left[f_i\left(t - \frac{x}{\overline{c}_i}\right) - g_i\left(t + \frac{x}{\overline{c}_i}\right)\right] \tag{22}$$

We take Laplace transforms of the travelling waves, hence $f_i\left(t - \frac{x}{\overline{c}}\right) = F_i(s)\, e^{st}\, e^{-s\frac{x}{\overline{c}_i}}$ and $g_i\left(t + \frac{x}{\overline{c}}\right) = G_i(s)\, e^{st}\, e^{+s\frac{x}{\overline{c}_i}}$. The jump conditions between the elements model the visco-thermal phenomena in the system. The first is the heat and momentum transfer that occurs in the boundary layer due to velocity and temperature gradients at the tube walls and around the heater prongs and wires. The second is the heat and momentum transfer where the heater and thermocouples are inserted. The third is the thermoacoustic mechanism, which we deal with separately in Sec. 6. The radiation of acoustic energy through the tube ends is accounted for by a reflection coefficient, experimentally calculated and assumed to be constant for all the experiments.

The visco-thermal drag in the boundary layer is distributed inside each acoustic element. From [10], the fluctuating wall shear stress is $\tau_{wall} = -(\rho\nu/\delta_{bl})u'$, where $\delta_{bl} = 2\pi(2\nu/s_i)^{1/2}$. Consider now an element of tube with length Δx and total perimeter πD_Σ, with $D_\Sigma = D + 2(D_p + D_w)$. This diameter allows us to account for the presence of the two prongs and wires to which the heater is attached. The total fluctuating force on the fluid element is

$$\Delta F = \Delta x\, \pi D_\Sigma\, \tau_{wall} = -\Delta x\, D_\Sigma \frac{\rho}{2^{3/2}}(s_i\nu)^{1/2}u' \tag{23}$$

We now define an equivalent area, and corresponding equivalent diameter, to account for a reduced flow area in the acoustic elements that contain heater prongs and wires:

$$A_e = A - A_p - A_w = \frac{\pi}{4}(D^2 - 2D_p^2 - 2D_w^2) = \frac{\pi}{4}D_e^2 \tag{24}$$

(If an acoustic element does not contain heater prongs and wires, then we set $D_\Sigma = D_e = D$ and $A_e = A$.) Integrating the momentum equation across adjacent acoustic elements gives the pressure jump as a known linear function of the acoustic velocity u'

$$\begin{aligned} p'_{i+1}(t) - p'_i(t) &= \frac{\Delta F(t)}{A_e} \\ &= -\Delta x \frac{D_\Sigma}{\pi D_e^2}\rho(2\nu s_i)^{1/2}u'_i(t) \\ &\equiv -k_{vis,bl}u'_i(t) \end{aligned} \tag{25}$$

Similarly, the heat transfer from the wall into the gas is

$$\Delta\dot{q} = -\Delta x\, \pi D_\Sigma \frac{\lambda}{\delta_{\mathrm{bl}}} T' \tag{26}$$

where δ_{bl} is assumed to be the same as for the viscous boundary layer because the Prandtl number for air is close to 1. The gas is assumed isentropic and ideal, so $\frac{T'}{T} = \frac{p'}{p}\frac{\gamma-1}{\gamma}$ and $p = \rho R_{\mathrm{g}}^* T$. By combining the previous relationships, we obtain the heat transfer as a known linear function of the acoustic pressure p':

$$\Delta\dot{q} = -\Delta x\, D_\Sigma \frac{(s_{\mathrm{i}}\nu)^{1/2}}{2^{3/2}\mathrm{Pr}}\, p' \tag{27}$$

This can be written as a jump condition for the acoustic velocity. Integrating the energy equation across adjacent acoustic elements gives

$$\begin{aligned} u'_{\mathrm{i}+1}(t) - u'_{\mathrm{i}}(t) &= \frac{\gamma-1}{\gamma}\,\frac{1}{p}\,\frac{4}{\pi D_{\mathrm{e}}^2}\Delta\dot{q}(t) \\ &= -\Delta x\,\frac{\gamma-1}{\gamma}\,\frac{1}{p}\,\frac{(s_{\mathrm{i}}\nu)^{1/2}}{2^{3/2}\mathrm{Pr}}\, p'_{\mathrm{i}}(t) \\ &\equiv -k_{\mathrm{th,bl}} p'_{\mathrm{i}}(t) \end{aligned} \tag{28}$$

By combining Eqs. (21), (22), (25) and (28), the momentum and energy jump conditions at x_{dd} can be written in terms of F and G as

$$\begin{aligned} &F_{\mathrm{i}+1} e^{-s\frac{x_{\mathrm{dd}}}{\bar{c}_{\mathrm{i}+1}}} + G_{\mathrm{i}+1} e^{+s\frac{x_{\mathrm{dd}}}{\bar{c}_{\mathrm{i}+1}}} - F_{\mathrm{i}}\left(1 - \frac{k_{\mathrm{vis,bl}}}{\bar{\rho}_{\mathrm{i}}\bar{c}_{\mathrm{i}}}\right) e^{-s\frac{x_{\mathrm{dd}}}{\bar{c}_{\mathrm{i}}}} \\ &- G_{\mathrm{i}}\left(1 + \frac{k_{\mathrm{vis,bl}}}{\bar{\rho}_{\mathrm{i}}\bar{c}_{\mathrm{i}}}\right) e^{+s\frac{x_{\mathrm{dd}}}{\bar{c}_{\mathrm{i}}}} = 0 \end{aligned} \tag{29}$$

$$\begin{aligned} &F_{\mathrm{i}+1}\frac{e^{-s\frac{x_{\mathrm{dd}}}{\bar{c}_{\mathrm{i}+1}}}}{\bar{\rho}_{\mathrm{i}+1}\bar{c}_{\mathrm{i}+1}} - G_{\mathrm{i}+1}\frac{e^{+s\frac{x_{\mathrm{dd}}}{\bar{c}_{\mathrm{i}+1}}}}{\bar{\rho}_{\mathrm{i}+1}\bar{c}_{\mathrm{i}+1}} \\ &+ F_{\mathrm{i}}\left(k_{\mathrm{th,bl}} - \frac{1}{\bar{\rho}_{\mathrm{i}}\bar{c}_{\mathrm{i}}}\right) e^{-s\frac{x_{\mathrm{dd}}}{\bar{c}_{\mathrm{i}}}} \\ &+ G_{\mathrm{i}}\left(k_{\mathrm{th,bl}} + \frac{1}{\bar{\rho}_{\mathrm{i}}\bar{c}_{\mathrm{i}}}\right) e^{+s\frac{x_{\mathrm{dd}}}{\bar{c}_{\mathrm{i}}}} = 0 \end{aligned} \tag{30}$$

For the first and last acoustic elements

$$F_1 e^{-s\frac{x_{\mathrm{u}}}{\bar{c}_1}} - R_1 G_1 e^{+s\frac{x_{\mathrm{u}}}{\bar{c}_1}} = 0 \tag{31}$$

$$R_2 F_{\mathrm{N}} e^{-s\frac{x_{\mathrm{d}}}{\bar{c}_{\mathrm{N}}}} - G_{\mathrm{N}} e^{+s\frac{x_{\mathrm{d}}}{\bar{c}_{\mathrm{N}}}} = 0 \tag{32}$$

Eqs. (29) to (32) can be written in matrix form as

$$\mathbf{A}(s)\mathbf{W} = \mathbf{0} \tag{33}$$

where s is the complex frequency of the system, whose real and imaginary parts represent growth rate and frequency of the thermoacoustic oscillations. $\mathbf{W}$ is the vector of complex amplitudes $[F_{\mathrm{i}}, G_{\mathrm{i}}]^T$, with $i = 1, \ldots, N$, and N the total number of acoustic elements. Further modelling is described in the following section, where some results are presented.

5.2 Analysis

The decay rate and frequency of oscillations in the empty tube, averaged over 1100 identical experiments, are $s = -7.61\ \mathrm{rad\cdot s^{-1}} + i\ 168.10$ Hz. We assume that the two ends are acoustically identical, i.e. $R_1 = R_2 = R$, and solve Eq. (33) for R, given s. This gives a reflection coefficient for the empty tube of $R = -0.9758 + i\ 0.1003$. Once the reflection coefficient is known, the heater is placed inside the tube at different positions, without switching it on. The following 11 positions are investigated: $x_{\mathrm{h}}/L = [0.55, 0.50, 0.45, 0.40, 0.35, 0.30, 0.25, 0.20, 0.15, 0.10, 0.01]$. For each case, 100 identical experiments are performed. The heater is modelled as a visco-thermal drag element with a time delay, following the theoretical analysis of [11] and knowledge of the qualitative form of the feedback sensitivities in [10]. Hence the jump conditions $\big($Eqs. (25) and (28)$\big)$ at the heater location are

$$p'_{\mathrm{i}+1}(t) - p'_{\mathrm{i}}(t) = -k_{\mathrm{vis,h}} u'_{\mathrm{i}}(t - \tau_{\mathrm{vis,h}}) \tag{34}$$

$$u'_{\mathrm{i}+1}(t) - u'_{\mathrm{i}}(t) = -k_{\mathrm{th,h}} p'_{\mathrm{i}}(t - \tau_{\mathrm{th,h}}) \tag{35}$$

The four parameters $k_{\mathrm{vis,h}}$, $k_{\mathrm{th,h}}$, $\tau_{\mathrm{vis,h}}$, and $\tau_{\mathrm{th,h}}$ are obtained by finding the best fit to Eqs. (33) to (35), given 100 measurements of s at each of the 11 heater positions.

Fig. 7 shows the predictions of the network model compared to the experimental measurements for all heater positions. The calibrated parameters are reported in the caption. The time of the viscous drag, $\tau_{\mathrm{vis,h}}$, is negative, while the thermal time delay, $\tau_{\mathrm{th,h}}$, is positive, in agreement with [11]. The pressure loss coefficient due to viscous drag at the heater location, $k_{\mathrm{vis,h}}$, is several orders of magnitude larger than the thermal loss coefficient, $k_{\mathrm{th,h}}$. Nevertheless, setting $k_{\mathrm{th,h}}$ to zero results in relatively large errors in Fig. 7, showing that the thermal transfer to the heater cannot be neglected, even when the heater is switched off.

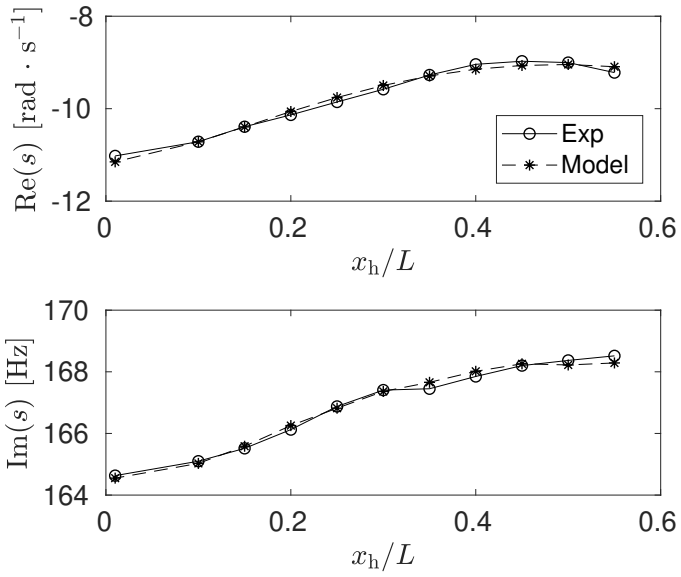

FIGURE 7: Decay rate (top) and frequency (bottom) of acoustic oscillations when the heater is switched off and placed at different x_h/L. The calibrated heater parameters are: $k_\mathrm{vis,h} = 27.3$ kg m^{-2} s^{-1}, $k_\mathrm{th,h} = 1.53 \cdot 10^{-5}$ kg^{-1} m^2 s, $\tau_\mathrm{vis,h} = -1.36 \cdot 10^{-3}$ s, and $\tau_\mathrm{th,h} = 8.98 \cdot 10^{-4}$ s.

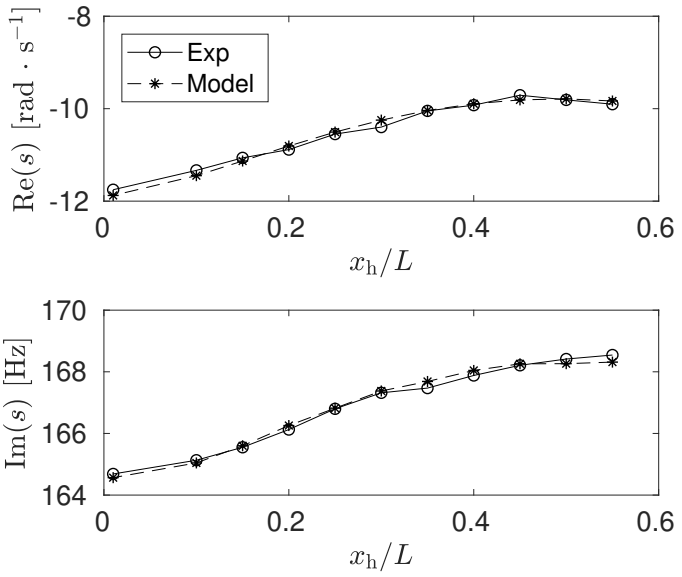

FIGURE 8: Decay rate (top) and frequency (bottom) of acoustic oscillations when the heater is switched off and placed at different x_h/L, and thermocouples present inside the tube. The calibrated thermocouple parameters are: $k_\mathrm{vis,t} = 0.257$ kg m^{-2} s^{-1}, $k_\mathrm{th,t} = 1.44 \cdot 10^{-7}$ kg^{-1} m^2 s.

We tried building several other models, which all failed to predict the correct trend. For example, we tested different combinations of models in which the pressure jump is proportional to p' or the velocity jump is proportional to u'. This is in perfect agreement with the predictions of the feedback sensitivities in [10] (see Fig 7a in [10]).

The 8 thermocouples are then placed in the tube and the decay rate and frequency of acoustic oscillations are measured with a further 100 experiments at each of the 11 heater positions. There is a small but noticeable shift in the decay rate (top of Figs. 7 and 8). We introduce 8 new jump conditions into the model, one at each thermocouple location. We then fix the ratio $k_\mathrm{vis,t}/k_\mathrm{th,t}$ to be the same as that of the heater, $k_\mathrm{vis,h}/k_\mathrm{th,h}$, and set the time delays to zero, for simplicity, so that the visco-thermal drag from the thermocouples is quantified by a single parameter. As before, we perform regression on Eq. (33) to calculate the optimal value of this parameter. This leads to accurate results, shown in Fig. 8, with the resulting best-fit parameters reported in the figure caption.

6 THERMOACOUSTIC MODEL COMPARISON

When the heater is switched on, in addition to accounting for the visco-thermal drag losses that occur in the boundary layer and across the heater and thermocouples (Sec. 5.2), one has to account for the thermoacoustic mechanism. By integrating Eq. (20) across the heater, the jump condition is

$$u'_{\mathrm{i}+1}(t) - u'_\mathrm{i}(t) = -k_\mathrm{th,h} p'(t-\tau_\mathrm{th,h}) + \frac{\gamma-1}{\gamma}\,\frac{1}{p}\,\frac{4}{\pi D^2}\dot{q}'_\mathrm{h}(t) \quad (36)$$

A common model for $\dot{q}'_\mathrm{h}(t)$ is the $n-\tau$ model [12], according to which the normalized heat release rate fluctuations are proportional to the normalized velocity fluctuations upstream of the heating element with a time delay:

$$\frac{\dot{q}'_\mathrm{h}(t)}{\dot{Q}_\mathrm{h}} = n\,\frac{u'_\mathrm{h}(t-\tau)}{U_1} \quad (37)$$

Assuming that the parameters n and τ in Eq. (37) are constant, one can do regression using the remaining 43200 experimental decay rates and frequencies at different heater powers in order to infer their values. One can then compare the performance of the model to the experiments. Results are shown in Fig. 9 and the best-fit parameters are reported in the figure caption. The agreement between the lines is fairly good and the main source of discrepancy occurs when predicting the frequency. The error becomes larger as the heater power increases. This is mainly because of the constant reflection coefficient assumed for this study. In reality, the phase of the reflection coefficient changes with the temperature, therefore, as the heater power increases, it

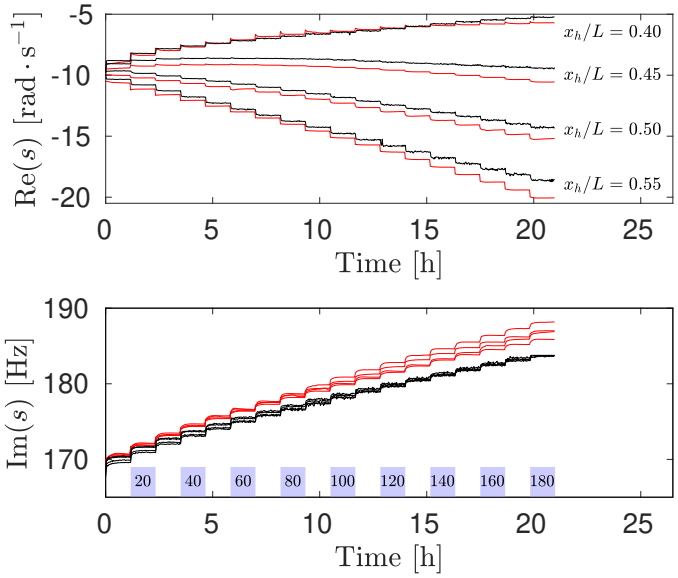

FIGURE 9: Decay rate (top) and frequency (bottom) of the oscillations for the case of heater switched on and placed at different x_h/L. The heater power is increased by 10 W every 70 minutes (bars at the bottom). Red lines: model. Black lines: experiments. Optimal thermoacoustic parameters: $n = 0.271$, $\tau = 0.517$ ms.

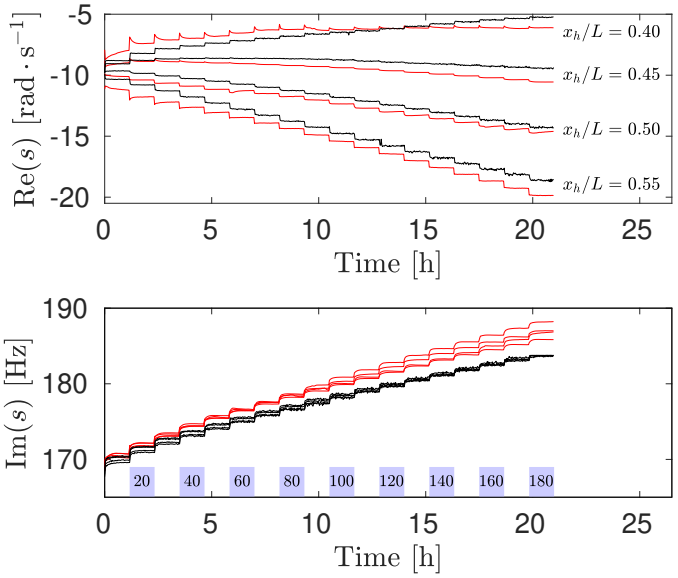

FIGURE 10: Decay rate (top) and frequency (bottom) of the oscillations for the case of heater switched on and placed at different x_h/L. The heater power is increased by 10 W every 70 minutes (bars at the bottom). Red lines: model. Black lines: experiments. Optimal thermoacoustic parameters: $n = 0.271$, $k_\tau = 2.04$.

is less and less valid to assume constant R_2 (Fig. 5f). On the other hand, the decay rate trend is correctly captured with fairly good accuracy for all the configurations.

The second model we propose is similar to Eq. (37) but τ is modelled as

$$\tau = k_\tau \frac{0.2 d_f}{U_1} \tag{38}$$

where d_f is the diameter of one of the many heater filaments (see Fig. 2), which is 0.559 mm. The choice of using this model takes inspiration from [11], who states that *"For frequencies small compared with $\omega_0 = 20\, U_1/d_f$, the departure of the heat-transfer fluctuations from their quasi-steady form consists essentially of a time lag of the order of $0.2\, d_f/U_1$"*. By doing regression over n and k_τ, one finds that the best-fit n does not change, whereas $k_\tau = 2.04$, which is close to the value of 1 implied by Lighthill's statement. With this value of k_τ, one obtains a time delay τ in the range $[0.45 - 1.20]$ ms. The results are plotted in Fig. 10. The frequencies predicted by the network model are similar to those in Fig. 9. The modelled decay rates, however, seem to be negatively affected by the dependence on velocity, especially at low powers, where the velocity shows significant transients (see Fig. 5d). Overall, the first model, where n and τ are assumed to be constant, seems to perform slightly better.

7 CONCLUSIONS

In this paper we use Bayesian inference on a thermoacoustic system and assimilate 324,000 temperature measurements and 46,500 decay rates/frequencies to infer the parameters of a reduced order model. The experiment consists of an electrically-heated Rijke tube in the thermoacoustically stable regime. Every 7 seconds we acoustically pulse the system with a loudspeaker at the bottom of the tube, and measure the subsequent decay rate and frequency with six probe microphones, sampling at 10 kHz. We measure the temperature of the air inside the tube at 8 axial locations, and use these data with their uncertainty to improve the predictions of an unsteady 1D conjugate heat transfer model for the base flow. For this, an Ensemble Kalman Filter with 30 members is used to provide statistically optimal estimates of state and parameters. This allows us to compute the inlet bulk velocity and the gas temperature at every grid point. The base flow model informs an acoustic network model, made up of 40 drag devices to account for visco-thermal losses in the boundary layer, and 9 drag devices to account for visco-thermal losses across the heater and the 8 thermocouples. We perform 1100 identical experiments with the empty tube in order to compute the reflection coefficients at the top and bottom ends, assuming them to be acoustically identical. We then place the heater inside the tube at 11 different locations without switching it on, and perform 100

identical experiments for every heater position. This allows us to infer the model parameters of the visco-thermal losses across the heater. We find that the viscous loss is characterized by a negative time delay, whereas the thermal loss has a positive time delay, in agreement with what found by [11]. We repeat the same procedure after placing the thermocouples inside the tube and work out through regression the influence of the thermocouples on the acoustic flow and thermal fields. Finally, we perform experiments with the heater switched on and investigate four different heater positions. We vary the heater power by 10 W every 70 minutes. We use the parameters learned in the cold tube cases to learn the parameters of two thermoacoustic models we propose: a classical $n-\tau$ model with constant parameters, and a modified version from [11], in which $\tau = k_\tau(0.2\,d_\mathrm{f})/U_1$.

This paper shows that an Ensemble Kalman Filter of many conjugate heat transfer simulations can assimilate experimental data from a rig, even if it never reaches steady state. Without this assimilation, the sound speed in a corresponding thermoacoustic network model is too inaccurate for the model to be quantitatively accurate. With this assimilation, combined with regression to infer another 7 parameters from 46,500 datapoints, a quantitatively accurate thermoacoustic model can be created. Although not shown here, several other models were tried, all of which failed to model the experimental data qualitatively, let alone quantitatively. Both heat release models perform well. Although we find that the first model performs slightly better than the second, we conclude that, as long as a model is qualitatively correct, it can be made quantitatively accurate over the range examined.

Further improvement of this method will be to infer the reflection coefficients with the multi-microphone method. This will allow us to account for the influence of the high temperature at the outlet end, which affects the phase of the reflection coefficient and, consequently, the model predictions of the oscillation frequency. We will also infer the parameters of more complex thermoacoustic models derived via system identification based on high-fidelity numerical simulations [13] in order to assess systematic model error (epistemic error). Another improvement will come from replacing regression with a more robust and quantitatively informative technique in order to provide uncertainty estimates also for the acoustic and thermoacoustic parameters. For this part of the work, a more natural choice than EnKF would be to use Markov Chain Monte Carlo, a Bayesian inference method that would allow us to relax the Gaussian distribution assumption albeit at a higher computational cost. In addition to this, in our future work we will train a purely data-driven machine learning algorithm and compare its performance to our physics-based statistical learning technique. Finally, investigating different configurations and acquiring new data will allow us to test whether a physics-based model can extrapolate in a reliable manner.

ACKNOWLEDGMENT

This project has received funding from the European Union's Horizon 2020 research and innovation programme under Grant Agreement No. 766264.

REFERENCES

[1] Oefelein, J. C., and Yang, V., 1993. "Comprehensive review of liquid-propellant combustion instabilities in F-1 engines". *Journal of Propulsion and Power,* ***9***(5), pp. 657–677.

[2] Lieuwen, T., and Zinn, B. T., 1998. "The role of equivalence ratio oscillations in driving combustion instabilities in low NO_x gas turbines". *Symposium (International) on Combustion,* ***27***(2), pp. 1809 – 1816.

[3] Candel, S. M., 2002. "Combustion dynamics and control: progress and challenges". *Proceedings of the Combustion Institute,* ***29***(1), pp. 1–28.

[4] Candel, S. M., 1992. "Combustion instabilities coupled by pressure waves and their active control". *Symposium (International) on Combustion,* ***24***(1), pp. 1277–1296.

[5] Evensen, G., 2009. *Data Assimilation: The Ensemble Kalman Filter*, 2nd ed. Springer.

[6] Rayleigh, J. W., 1878. "The explanation of certain acoustical phenomena". *Nature,* ***18***(455), pp. 319–321.

[7] Saito, T., 1965. "Vibrations of air-columns excited by heat supply". *The Japan Society of Mechanical Engineers,* ***8***(32), pp. 651–659.

[8] Jamieson, N. P., and Juniper, M. P., 2017. "Experimental sensitivity analysis of a linearly stable thermoacoustic system via a pulsed forcing technique". *Experiments in Fluids,* ***58***(9), p. 123.

[9] Aguilar, J. G., Magri, L., and Juniper, M. P., 2017. "Adjoint-based sensitivity analysis of low-order thermoacoustic networks using a wave-based approach". *Journal of Computational Physics,* ***341***, pp. 163–181.

[10] Juniper, M. P., 2018. "Sensitivity analysis of thermoacoustic instability with adjoint helmholtz solvers". *Physical Review Fluids,* ***3***(11), p. 110509.

[11] Lighthill, M. J., 1954. "The response of laminar skin friction and heat transfer to fluctuations in the stream velocity". *Proceedings of the Royal Society of London A: Mathematical, Physical and Engineering Sciences,* ***224***(1156), pp. 1–23.

[12] Crocco, L., 1969. "Research on combustion instability in liquid propellant rockets". *Symposium (International) on Combustion,* ***12***(1), pp. 85 – 99.

[13] Witte, A., 2018. "Dynamics of unsteady heat transfer and skin friction in pulsating flow across a cylinder". PhD thesis, Technische Universität München.